

## Article

# Simulation Analysis of the Safety of High-Energy Hydroxyl-Terminated Polybutadiene (HTPB) Engine under the Impact of Fragments

Zheng Liu <sup>1</sup>, Jianxin Nie <sup>1,\*</sup>, Wenqi Fan <sup>2</sup>, Jun Tao <sup>3</sup>, Fan Jiang <sup>3</sup>, Tiejian Guo <sup>4</sup> and Kun Gao <sup>4</sup><sup>1</sup> State Key Laboratory of Explosion Science and Technology, Beijing Institute of Technology, Beijing 100081, China<sup>2</sup> School of Aerospace Engineering, Tsinghua University, Beijing 100084, China<sup>3</sup> Xi'an Modern Chemistry Research Institute, Xi'an 710065, China<sup>4</sup> Xi'an Changfeng Research Institute of Mechanical-Electrical, Xi'an 710065, China

\* Correspondence: niejx@bit.edu.cn

**Abstract:** The safety of solid rocket engine use seriously affects the survivability and combat effectiveness of weaponries. To study the engine safety against fragment in complex battlefield environments, the fragment impact safety simulation study of a high-energy four-component HTPB propellant solid engine (hereafter referred to as high-energy HTPB propellant engine) was conducted. The equation of state parameters and reaction rate equation parameters of the detonation product of high-energy HTPB propellant were calibrated by using a 50 mm diameter cylinder test and Lagrange test combined with genetic algorithm. The nonlinear dynamics software LS-DYNA was used to build a finite element model of the fragment impact engine and simulate the mechanical response of the high-energy HTPB propellant under different operating conditions. This study shows that the critical detonation velocity decreases with the increase of the number of fragments. When the number of fragments is more than 5, the influence of this factor on the critical detonation velocity is no longer obvious. Under the same loading strength conditions, the greater the metal shell strength and the greater the shell wall thickness, the more difficult it is for the high-energy HTPB propellant to be detonated by the shock. This study can provide a reference for the design and optimization analysis of solid rocket engine fragment impact safety.



**Citation:** Liu, Z.; Nie, J.; Fan, W.; Tao, J.; Jiang, F.; Guo, T.; Gao, K. Simulation Analysis of the Safety of High-Energy Hydroxyl-Terminated Polybutadiene (HTPB) Engine under the Impact of Fragments. *Crystals* **2023**, *13*, 394. <https://doi.org/10.3390/cryst13030394>

Academic Editor: Thomas M. Klapötke

Received: 8 February 2023

Revised: 21 February 2023

Accepted: 21 February 2023

Published: 24 February 2023



**Copyright:** © 2023 by the authors. Licensee MDPI, Basel, Switzerland. This article is an open access article distributed under the terms and conditions of the Creative Commons Attribution (CC BY) license (<https://creativecommons.org/licenses/by/4.0/>).

**Keywords:** safety engineering; fragmentation impact; high-energy HTPB propellant; shock initiation; equation of state

## 1. Introduction

Composite solid propellants have been widely used in modern rocket engines, missile engines, rocket boosters and other power devices since the 1840s. As a typical composite propellant, high-energy HTPB propellant has the advantages of excellent combustion performance and mechanical properties, low flame temperature, low molecular combustion products and low infrared radiation. However, it also has a high probability of detonation and the risk of detonation. To improve the specific impulse and other performance, the proportion of nitramine propellant continued to increase, which reduced the critical detonation diameter of the nitramine composite propellant. This leads to an increased possibility of accidental explosive accidents during the actual assembly, storage, transportation and operation of the engine, posing a great threat to personnel safety and the environment. Therefore, it is extremely important to study the critical conditions for the occurrence of hazardous reactions of solid rocket motors under the action of impact loads [1].

The detonation safety of solid propellants began to be researched early. The research contains the critical diameter of the propellant [2], impact initiation [3–6], combustion to detonation [7–9] and other aspects. The detonation parameters are mainly focused on the study of the detonation velocity. Hot spot theory was first proposed by Bowden

and other scholars [10] in 1948. HTPB four-component propellant as a nonhomogeneous explosive, and the formation of hot spots is currently considered to be the cause of its initiation of shock detonation. Price et al. [11] found that AP/Al/1,3,5,7-tetranitro-1,3,5,7-tetrazocane(HMX)/Wax propellants exhibit the properties of a second type of explosive, and the critical diameter of the propellant for detonation becomes larger as the charge porosity decreases. Dick [12] conducted a wedge test to study the detonation process of different formulations of AP/Al/HMX/Wax propellants. The tests showed that propellants with HMX content less than 20% could not be shock-detonated to produce a self-sustaining burst; when the HMX content was 44%, the detonation behavior of the propellants approximated that of high-energy explosives. Baker et al. [4] conducted a drop hammer experiment to obtain the impact sensitivities and critical impact initiation energies of three HTPB-based propellants. It was shown that the propellants were detonated only when the propellant nitramine content was high and when the critical detonation energy of the propellants was high. Kohga et al. [13] showed that the detonation velocity of ammonium nitrate (AN)/nitroamine-based composite propellant increases linearly with the increase in the mass of nitramine within the unit volume of propellant, and the effect of AN on the detonation performance can be ignored. In 1991, Bai et al. [14] studied the chemical reaction process of various solid propellants, including butyl hydroxyl propellants, under different pressure shock waves for the first time in China based on the Lagrangian test. Yang et al. [15] conducted numerical simulations of the process of flat plate breakers impacting flat shells, adiabatic layers and propellants. Li et al. [16] conducted a more comprehensive combination of low susceptibility propellant studies under mechanically stimulated conditions such as bullet impact and fragment impact.

In summary, the high nitramine content of the composite propellant blast work capacity, especially the blast-driven metal acceleration capacity, is less studied. Although the main components of nitramine composite propellants and plastic-bonding explosives (PBX) are similar, they generally have a higher ammonium perchlorate (AP) content and lower nitramine content; the detonation process is nonideal. Therefore, the existing studies of PBX explosive burst-driven metal acceleration capability are not sufficient to support the characterization of the detonation performance of nitramine composite propellants. There is a lack of basic test data to support solid rocket engine detonation hazard assessment.

To deal with the safety of the engine against fragmentation impact in a complex battlefield environment, a 50 mm cylinder test and Lagrange test of high-energy HTPB propellant were designed and completed. The parameters of its equation of state were calibrated by using a genetic algorithm. The nonlinear dynamics software LS-DYNA was applied to build a fragment impact engine model and simulate the mechanical response characteristics of the high-energy HTPB engine under different operating conditions. The results of this study can provide references for the design and optimization analysis of the fragment impact safety of solid rocket engines.

## 2. High-Energy HTPB Propellant Equation of the State Calibration Test

### 2.1. Cylinder Experiment

In this paper, the high-energy four-component HTPB propellant was studied with the following components: AP/Al/cyclotrimethylenetrinitramine(RDX)/HTPB = 50/5/30/15. The density of the propellant was  $1.645 \text{ g/cm}^3$ . The propellant was tested on a copper tube with a diameter of  $\Phi 50 \text{ mm}$ , and the test configuration is shown in Figure 1. Figure 1a shows the schematic diagram of the cylinder test, and Figure 1b shows the cylinder test configuration. The cylinder experiment device consisted of high-voltage electric detonator, detonating column, copper tube, composite propellant, electric probe, Photonic Doppler Velocimetry (PDV) and a bracket. The  $\Phi 50 \text{ mm}$  cylinder was placed vertically on the stand, and the cylinder expansion velocity was tested by laser interference velocimetry at a height of 200 mm during the stable detonation stage of the explosive.

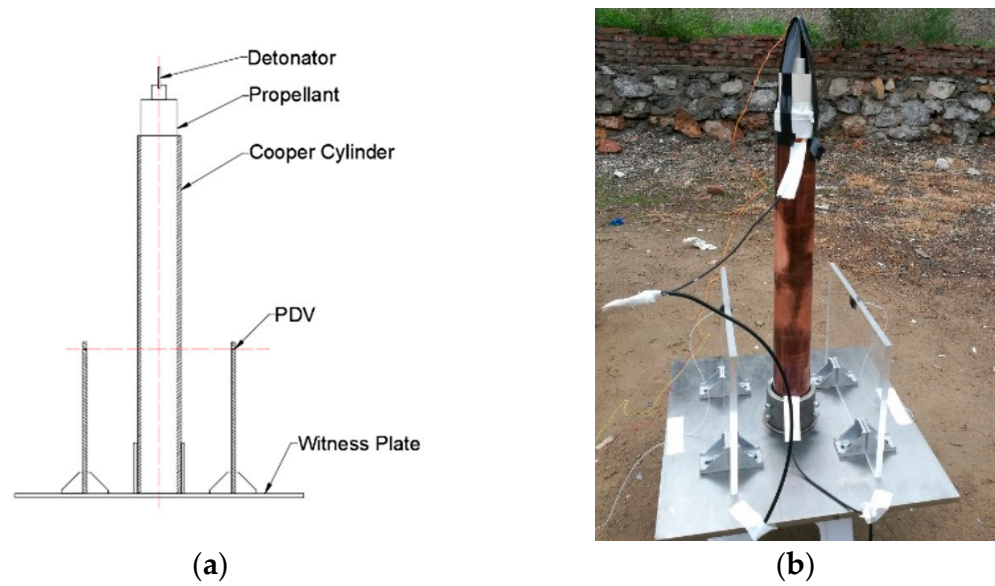


**Figure 1.** Schematic diagram of cylinder test. (a) Cylinder test design diagram. (b) Cylinder test configuration diagram.

The outer diameter of the copper tube was  $\Phi 60$  mm and the inner diameter was  $\Phi 50$  mm. The length of the copper tube was 495 mm, and the material was high conductivity oxygen-free copper. The detonation velocity of the composite propellant was measured using ionization probes fixed at both ends of the cylinder, and the distance between the two ionization probes was 495 mm. The recording frequency of the PDV was 24.4 MHz.

2.2. Lagrange Test

The high-energy HTPB four-component propellant used in this section remains the same as in section A. In order to ensure the uniformity of the material, firstly, the high-energy HTPB four-component propellant pillar was cut into tablets from the cast molding (the thickness of the tablets was divided into three series: 2~3 mm, 5 mm and 30 mm, which were reasonably matched according to the designed test position), and then the propellant tablets were cut into uniform diameter pillars with a  $\Phi 50$  mm circular cutter. The design and assembly diagram of the test device are shown in Figure 2.

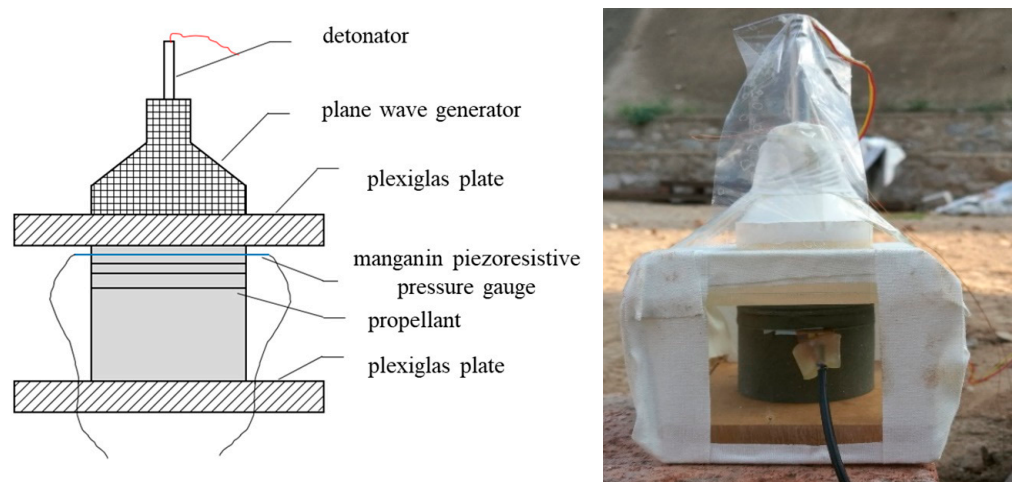


**Figure 2.** Design diagram and assembly diagram of Lagrange test device.

Among them, the plane wave generator was press-fitted by an 8701 explosive and a TNT explosive. The plexiglass plate was 8 cm × 10 cm square plate with thickness of 18.0 mm. The sensor adopts H-type manganin piezoresistive sensor.

### 2.3. Test Results and Analysis

#### 2.3.1. Cylinder Test Results and Analysis

After the cylinder expansion experiment, the witness plate was perforated. As can be seen from Figure 3, the thickness of the 5 mm steel witness plate was perforated, and the perforation diameter reached  $\Phi 93.80$  mm, indicating that the high-energy four-component HTPB propellant occurred in the form of a stable detonation reaction.

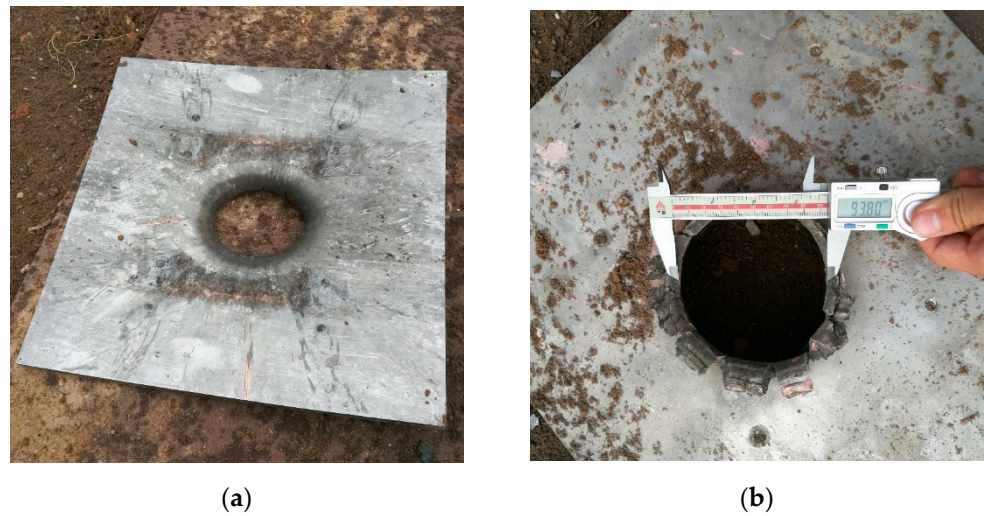


**Figure 3.** Shape of witness plate perforation after cylinder expansion experiment. (a) Witness plate front. (b) Back of the witness plate.

The detonation velocity of the composite propellant can be measured by the electric probes added at both ends of the cylinder. Figure 4 gives the electric probe pulse signal curve of the four-component HTPB propellant. The first sharp pulse in the curve is the upper surface of the copper tube at the pillar clamped electric probe signal; the second sharp pulse is the lower surface of the copper tube at the pillar clamped ionization probe. The time difference between the two signals is the stable detonation propagation time  $\Delta\tau$  in the copper tube.

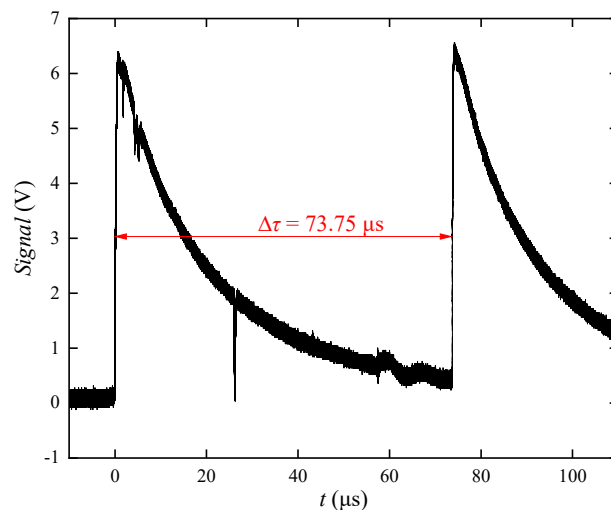


**Figure 4.** Velocity signal of four-component HTPB propellant.

The distance between the two ionization probes was  $d = 495 \text{ mm}$ , and the time difference between the two electric probe signals was  $\Delta\tau = 73.75 \text{ }\mu\text{s}$ . This can be calculated to obtain the detonation velocity of four-component HTPB propellant  $V = 6712 \text{ m/s}$ . The detonation pressure  $P_{CJ}$  of the composite propellant can be calculated with the following equation.

$$P_{CJ} = \frac{1}{\gamma + 1} \rho_0 V^2 \tag{1}$$

where  $\rho_0$  is the charge density of the propellant;  $V$  is the detonation velocity of the propellant; and  $P_{CJ}$  is the detonation pressure of the propellant. In general, assuming  $\gamma = 3$ , it can be calculated to obtain the detonation pressure of HTPB propellant  $P_{CJ} = 18.53 \text{ GPa}$ .

### 2.3.2. Lagrange Test Results and Analysis

Six Lagrange tests were conducted, and the actual Lagrange point locations are shown in Table 1.

**Table 1.** Actual Lagrange point location for Lagrange test.

Actual Insertion Position/ $x_i$	$x_1/\text{mm}$	$x_2/\text{mm}$	$x_3/\text{mm}$	$x_4/\text{mm}$	$x_5/\text{mm}$	$x_6/\text{mm}$
Distance from Plexiglas plate position	0.00	3.10	5.69	8.43	14.24	20.12

The voltage data obtained at each Rasch point were subjected to data noise reduction and smoothing. The obtained pressure time course curves are shown in Figure 5.

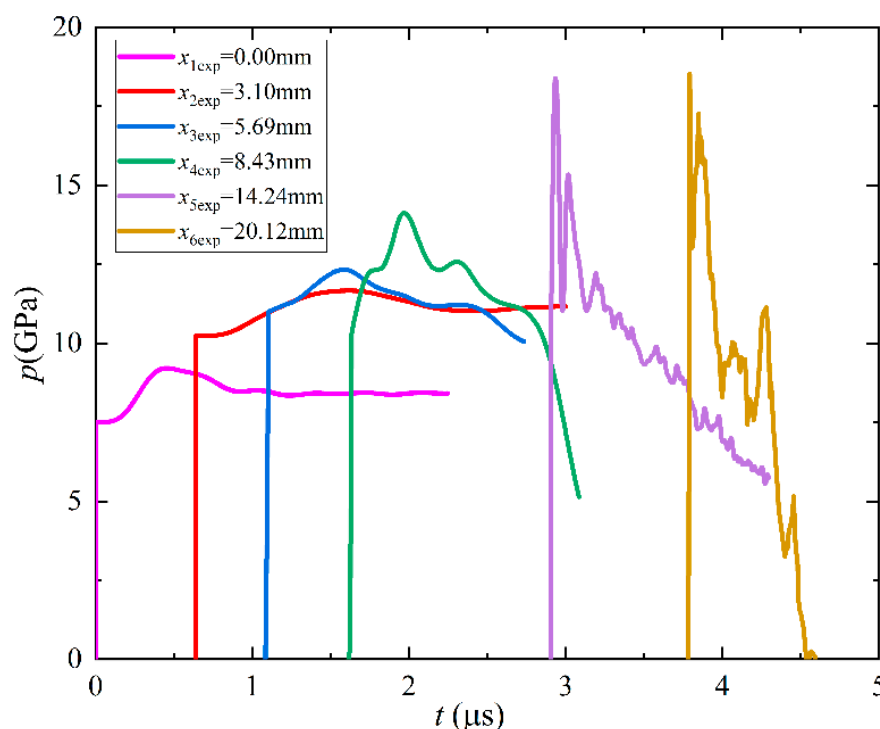


**Figure 5.** Pressure measurement data at each point of the Lagrange test.

### 2.4. Detonation Product Equation of State and Reaction Rate Equation Parameter Calibration

The Jones–Wilkson–Lee (JWL) [17] equation of state is commonly used to simulate the solid propellant detonation process, and the standard form of the equation is

$$p_s = A \left( 1 - \frac{\omega}{R_1 V} \right) e^{-R_1 V} + B \left( 1 - \frac{\omega}{R_2 V} \right) e^{-R_2 V} + \frac{\omega E_0}{V} \tag{2}$$

where  $p_s$  is the detonation product pressure;  $E_0$  is the volume specific internal energy;  $V$  is the relative specific volume of the detonation product; and  $A, B, R_1, R_2$  and  $\omega$  are constants, determined by the cylinder experiment.

The propellant is a typical nonhomogeneous explosive, so its shock initiation process and shock to detonation (SDT) can be analyzed by using the classical hot-spot theory. Lee and Tarver [18] proposed the ignition growth model in 1980, which has been improved and refined, and the model was widely accepted and applied. The ignition growth reaction rate model is

$$\begin{aligned} \frac{\partial \lambda}{\partial t} = & I(1 - \lambda)^b \left( \frac{\rho}{\rho_0} - 1 - a \right)^x H(F_{ig\max} - \lambda) \\ & + G_1(1 - \lambda)^c \lambda^d p^y H(F_{G1\max} - \lambda) \\ & + G_2(1 - \lambda)^e \lambda^f p^z H(\lambda - F_{G2\min}) \end{aligned} \tag{3}$$

where  $\lambda$  is the reactivity;  $H(x)$  is the step function; parameter  $I$  characterizes the number of hot-spots; parameter  $b$  is the order of combustion; parameter  $a$  is the critical compression of ignition; parameter  $x$  is the ignition term duration function;  $F_{ig\max}$  controls the maximum applicable reactivity of the ignition term; parameters  $G_1$  and  $d$  define the reaction growth rate of the hot-spot early after ignition; parameter  $c$  is the order of combustion of the growth term; parameter  $y$  is the pressure index;  $F_{G1\max}$  controls the maximum applicable reactivity of the growth term; parameters  $G_2$  and  $f$  define the reaction growth rate of the late hot-spot after ignition; parameter  $e$  is the combustion order of the completion term; parameter  $z$  is the pressure index; and  $F_{G2\min}$  controls the minimum applicable reactivity of the completion term.

#### 2.4.1. Calibration Process

In this paper, an adaptive genetic algorithm (AGA) was used to optimize the calibration process of the detonation product parameters. The algorithm can be used to obtain the global optimal fit parameters faster. The flow chart of the calibration equation of state parameters in this paper is shown in Figure 6.

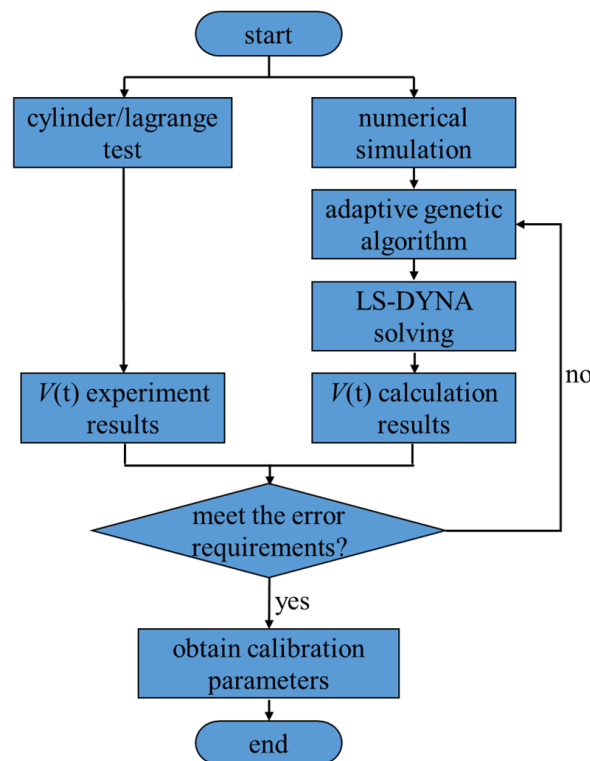
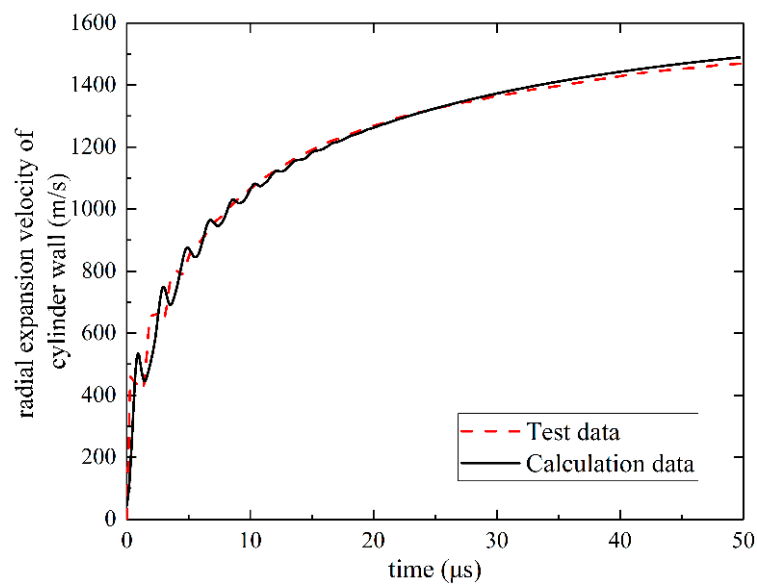


Figure 6. Flow chart of parameters calibration.

As shown in the figure, the initial parameter values are given by using an adaptive genetic algorithm. The radial expansion displacement curve is obtained by numerical simulation of nonlinear dynamics, and the curve is compared with the radial expansion displacement curve obtained experimentally to obtain the goodness of fit. Genetic operations are performed to generate a new generation population based on the fit values. Iterative calculations are performed to finally obtain the fitted parameters of the equation of state with a good degree of fit.

#### 2.4.2. Calibration Results

The parameters are calibrated and calculated by an adaptive genetic algorithm. As shown in Figures 7 and 8, the comparison of the cylinder wall radial expansion velocity and cylinder wall radial expansion displacement with the experimental data was obtained by simulation.



**Figure 7.** Wall velocity versus time curve of cylinder test.

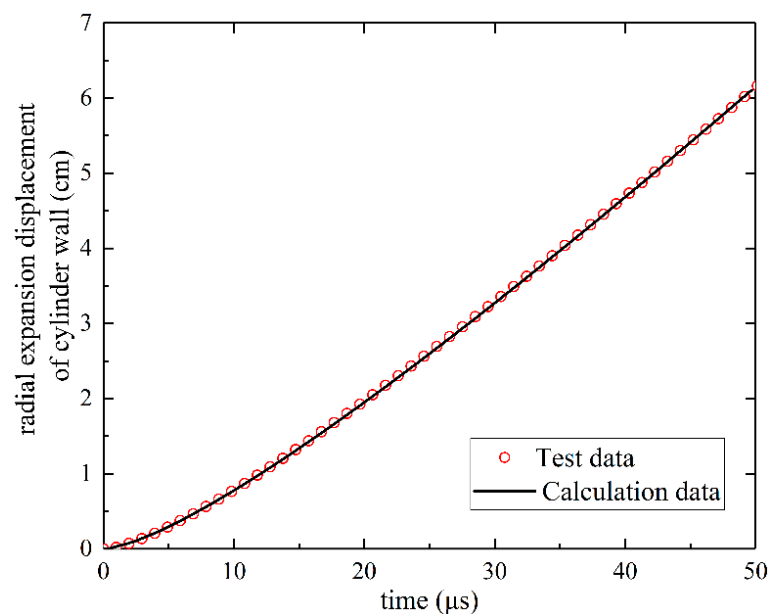


**Figure 8.** Wall displacement versus time curve of cylinder test.

The final obtained four-component HTPB propellant detonation product equations of state parameters are shown in Table 2.

**Table 2.** Propellant detonation product equations of state parameters.

$\rho_0$	$A/\text{GPa}$	$B/\text{GPa}$	$C/\text{GPa}$	$R_1$	$R_2$	$\omega$	$E_0/(\text{kJ}\cdot\text{cm}^{-3})$
1.645	481.34	4.5519	2.019	4.6916	1.6287	0.2796	0.0938

The pressure growth process obtained from the test and the pressure growth process obtained from the simulation is shown in Figure 9. In general, the manganin piezoresistive sensor may be destroyed after measuring the shock wave takeoff pressure within the propellant due to the action of the detonation products. After this measured pressure, data validity is poor and does not reflect the actual pressure changes during the shock initiation. Therefore, generally only the starting pressure in the Lagrange test should be used to calibrate the parameters, and the subsequent pressure is generally no longer used for calibration.

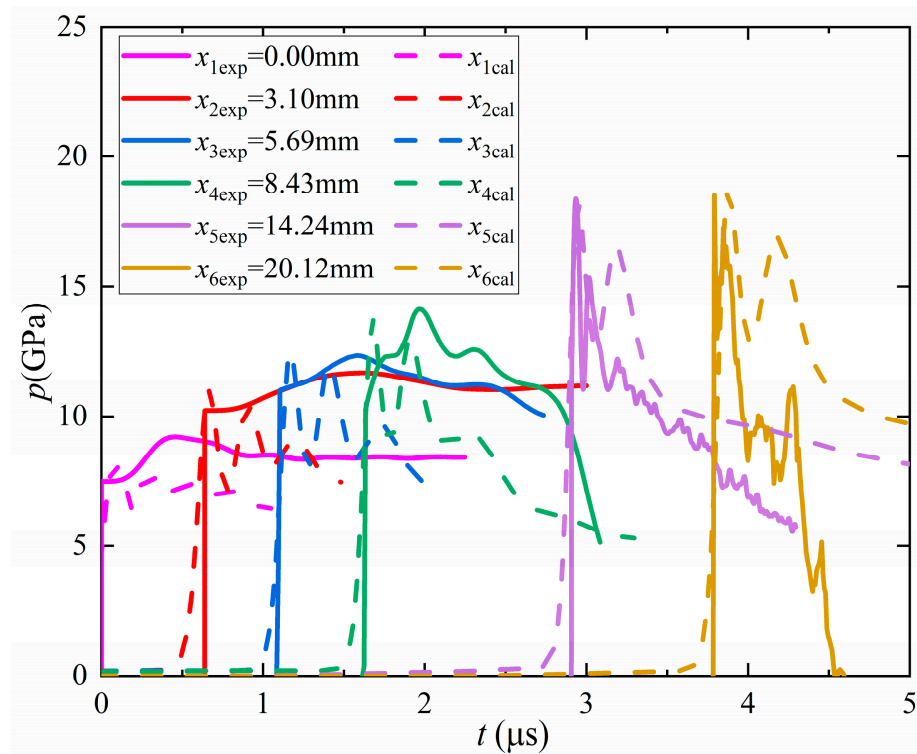


**Figure 9.** Comparison between the growth test and simulation calculation of the Lagrange test pressure.

The reaction rate parameters obtained for the final calibration are shown in Table 3.

**Table 3.** Parameters of high-energy HTPB four-component propellant reaction rate equation.

Parameter	Parameter Value	Parameter	Parameter Value	Parameter	Parameter Value
$I/\mu\text{s}^{-1}$	4427.1887	$G_1/(\text{GPa}^{-y}\cdot\mu\text{s}^{-1})$	1.8127	$G_2/(\text{GPa}^{-z}\cdot\mu\text{s}^{-1})$	261.7333
$a$	0.0248	$c$	0.6667	$e$	1.0
$b$	0.6667	$d$	0.1111	$f$	0.667
$x$	6.7385	$y$	1.0	$z$	2.0
$F_{ig\text{max}}$	0.01	$F_{G1\text{max}}$	1.0	$F_{G2\text{min}}$	0.0

### 3. Simulation of High-Energy HTPB Engine Fragmentation Impact Safety Experiment

#### 3.1. Simulation Model and Parameters

##### 3.1.1. Structural Model

A three-dimensional simulation model of the shell-loaded composite propellant loaded with different fragment impact velocities was established using TrueGrid parametric modeling software. The profile along the fragment impact direction is shown in Figure 10. The charge diameter of the high-energy HTPB propellant is  $\Phi 157$  mm, and the charge length is  $L = 400$  mm. The outer diameter of the shell is  $\Phi 160$  mm, the wall thickness of the shell is  $\delta = 1.5$  mm, and the length of the shell is  $L = 400$  mm. Standard breakers are used, and the propellant charge is loaded by positively impacting the shell in the direction perpendicular to the outer surface of the shell. The air domain radius is 2.5 times the propellant radius.

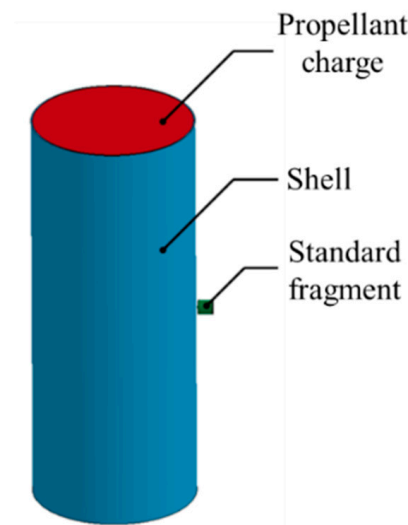


**Figure 10.** Schematic diagram of the standard fragmentation impact shell loading composite propellant model.

An arbitrary Lagrangian–Eulerian algorithm (ALE) was used to describe the high-energy HTPB propellant charge and the air unit. The Lagrangian algorithm was used to describe the metal shell and the fragmentation components. Among them, (a) the propellant cylindrical charge was modeled using the butterfly-type mesh modeling method, and the hexahedral cells were uniformly smoothed using the TrueGrid modeling method to make the cell mesh close to the orthogonal mesh. The accuracy of the calculation can be improved. Furthermore, (b) the hexahedral cells of the air model were also uniformly smoothed. The radius of the air domain was 2.5 times of the radius of the propellant, and the boundary was set as a reflection-free boundary to avoid the reflection of the wave at the boundary affecting the flow field calculation; (c) the metal shell adopted hexahedral cells, and five layers of cells were set in the thickness direction; (d) the standard breakers were 0.1 cm away from the outer wall of the shell. The breakers impacted the shell-mounted high-energy HTPB propellant in the vertical direction.

##### 3.1.2. Material Model

The response of different media under different loads is different. The material model is used in numerical simulation to define the relationship between the load and response of the medium. The instantonal model in the material model mainly describes the material stress–strain relationship, and the equation of state mainly describes the medium thermodynamic state relationship. Since the material model can hardly encompass all mechanical responses of the medium, a failure model can be attached when the medium is beyond the range of applicability of the material model. The material model of each component is shown in Table 4. The mechanical behavior and damage patterns of metallic

materials, such as breakers and shell materials, were described by the Johnson–Cook(J–C) material model. The equation of state of the impact process was described by the Gruneisen equation of state.

**Table 4.** Material model of each component.

Parts	Material Model	Equation of State	Failure Models
Propellant Charges	Fluid Elasticity Material Model	Ignition growth equation of state	/
Shell	J–C material model	Gruneisen equation of state	J–C failure model
Fragmentation	J–C material model	Gruneisen equation of state	J–C failure model
Air	Empty material model	Linear polynomial equation of state	/

The parameters of the metal material model used are shown in Table 5 [19,20].

**Table 5.** Metal material model parameters.

Materials	$\rho_0/(\text{g}\cdot\text{cm}^{-3})$	G/GPa	A/GPa	B/GPa	C	n	m	$T_m/K$
30CrMnSiA steel	7.85	75	0.525	0.101	0.1739	0.081	1.635	1800
45# steel	7.86	200	0.790	0.510	0.015	0.27	1.05	1800

Since the failure process of the shell is accompanied by the failure process of the shell during the impact of the standard fragments, this paper uses the J–C failure model and defines the failure strain as

$$\epsilon_f = \left( D_1 + D_2 e^{D_3 \sigma^*} \right) \left( 1 + D_4 \ln \dot{\epsilon}_{eq}^* \right) \left[ 1 + D_5 \left( 1 - e^{D_6 T^*} \right) \right] \tag{4}$$

where  $\epsilon_f$  represents the failure strain, and the unit is considered to fail when the strain of the material unit reaches this value;  $\sigma^*$ ,  $\dot{\epsilon}_{eq}^*$  and  $T^*$  represent the stress triaxiality, equivalent effect variability and temperature, respectively; and  $D_1$  to  $D_6$  are the damage parameters. The parameters of the J–C failure model for metallic materials in this section are shown in Table 6.

**Table 6.** Parameters of the J–C failure model for metallic materials.

Materials	$D_1$	$D_2$	$D_3$	$D_4$	$D_5$	$D_6$
30CrMnSiA steel	0.0705	1.732	−0.54	−0.0123	0	0
45# steel	0.78	0	0	0	0	0

The linear polynomial equation of state used for air is

$$p = C_0 + C_1 \mu + C_2 \mu^2 + C_3 \mu^3 + (C_4 + C_5 \mu + C_6 \mu^2) E \tag{5}$$

where  $p$  is the pressure;  $\mu$  is the compressibility;  $E$  is the internal energy; and  $C_0$  to  $C_6$  are the polynomial equation coefficients.

In addition, the JWL equation of state of unreacted propellant is essentially the unreacted impact equation of state of the composite material. To simplify the calculation, the equation of state for unreacted explosives was also expressed by using the JWL equation of state form:

$$p_u = A_u e^{-R_{1u} V_u} + B_u e^{-R_{2u} V_u} + \omega_u C_{V_u} T_u V_u^{-1} \tag{6}$$

where  $p_u$ ,  $V_u$  and  $T_u$  are the pressure, relative volume and temperature of the unreacted propellant, respectively;  $C_{V_u}$  is the constant volume of specific heat of the unreacted propellant;  $\omega_u$ ,  $A_u$ ,  $B_u$ ,  $R_{1u}$  and  $R_{2u}$  are the fitting constants of the equation of state.

It can be calculated by fitting the impact Hugoniot curve of the composite propellant. The fitting parameters are shown in Table 7.

**Table 7.** Parameters of equation of state for unreacted state high-energy HTPB propellant.

$A_u/\text{GPa}$	$B_u/\text{GPa}$	$R_{1u}$	$R_{2u}$	$\omega_u$	$C_{Vu}/(\text{GPa}\cdot\text{K}^{-1})$
36587.61	-2.789	11.0	0.4	1.69	$2.5 \times 10^{-3}$

### 3.2. Analysis of the Factors Affecting the Safety of the Standard Fragments Impact Engine

#### 3.2.1. Single Fragment

When  $v = 1830 \text{ m}\cdot\text{s}^{-1}$ , the impact detonation process of standard fragments impacting shell-loaded composite propellant is obtained by calculation, as shown in Figure 11.

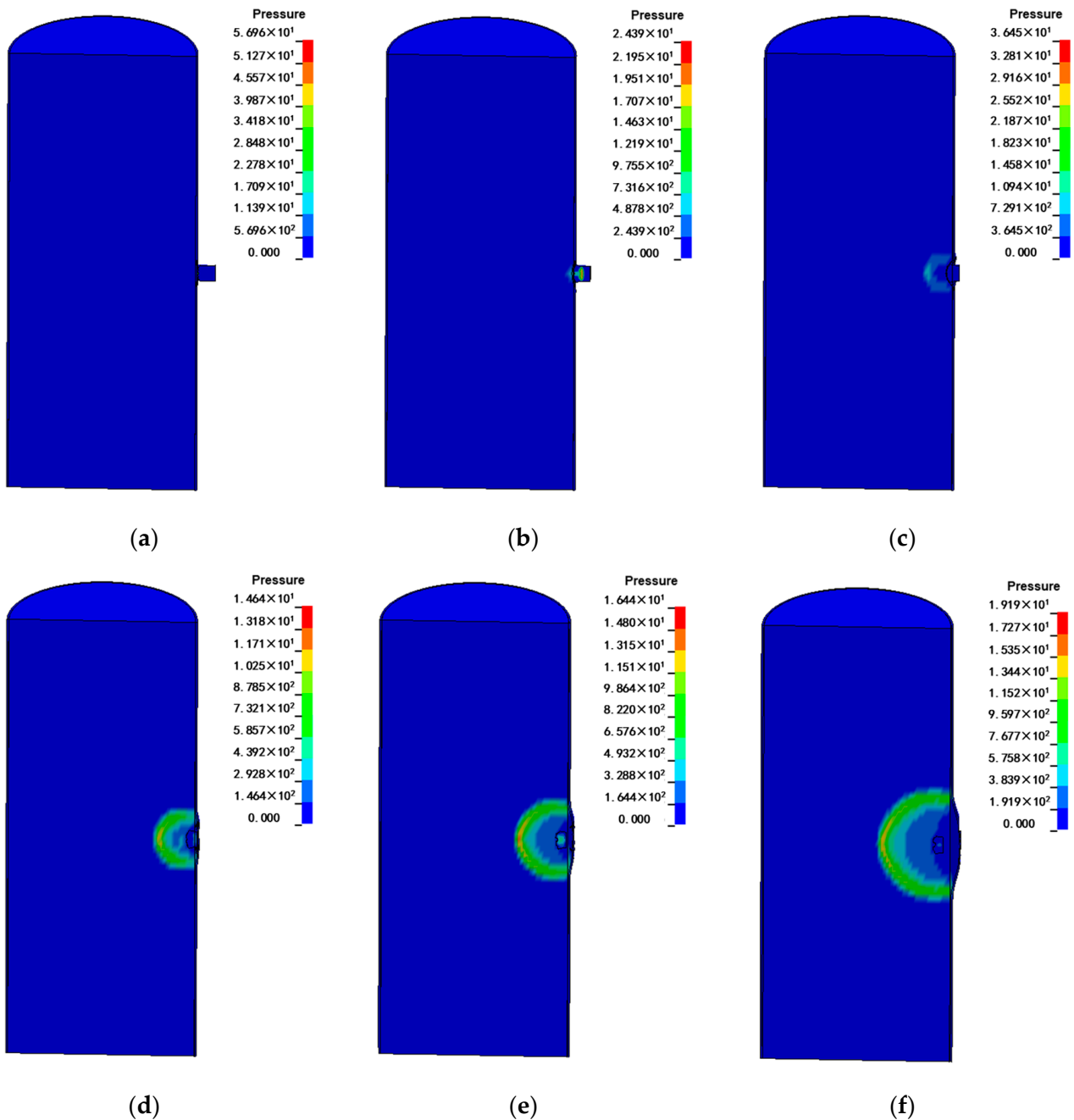


**Figure 11.** Internal pressure growth process when the propellant under the impact of the standard fragments of impact loading impact detonation. (a)  $t = 0.8 \mu\text{s}$ . (b)  $t = 2.4 \mu\text{s}$ . (c)  $t = 7.0 \mu\text{s}$ . (d)  $t = 9.0 \mu\text{s}$ . (e)  $t = 11.0 \mu\text{s}$ . (f)  $t = 13.8 \mu\text{s}$ .

Figure 11 shows that at  $t = 0.8 \mu\text{s}$  (a), a high-speed fragment with  $v = 1830 \text{ m}\cdot\text{s}^{-1}$  strikes the shell and generates a strong shock wave. At  $t = 2.4 \mu\text{s}$  (b), the shock wave generated by the impact propagates simultaneously in two opposite directions, radial direction of the shell and axial direction of the fragment. The metal shell at the impact is concaved and deformed under the action of the broken fragment. At  $t = 7.0 \mu\text{s}$  (c), the standard fragment penetrates the metal shell and comes into contact with the high-energy HTPB propellant charge. The shock wave within the propellant charge begins to propagate and excite the propellant reaction. At  $t = 9.0 \mu\text{s}$  (d), the fragment passes through the shell and penetrates the propellant charge. The pressure inside the propellant charge gradually increases. At  $t = 11.0 \mu\text{s}$  (e), the peak shock wave pressure within the propellant charge continues to rise, and the shell begins to expand outward driven by the explosion products at the perforation where the shell was struck. At  $t = 13.8 \mu\text{s}$  (f), a steady burst wave is generated within the propellant charge, and the burst wave continues to propagate within the propellant charge.

The critical detonation speed of the broken fragment impact is shown in Table 8.

**Table 8.** Fragmentation impact critical detonation velocity.

Shape of Fragment	Density $\rho_0/(\text{g}\cdot\text{cm}^{-3})$	Characteristic Size of the Fragment $l/(\text{mm})$	Critical Detonation Velocity $V_{cr}/(\text{m}\cdot\text{s}^{-1})$
Standard fragment	7.86	14.3	1550

### 3.2.2. Multiple Fragment

In the martyrdom process, solid rocket motors are often subjected to the joint action of many fragments. By establishing a simulation model of multiple fragment impact on shell-mounted composite propellant, the critical detonation velocity is obtained under different numbers of standard fragment impacting at equal intervals in the longitudinal direction. The variation of the critical impact velocity with the number of fragments is shown in Figure 12.

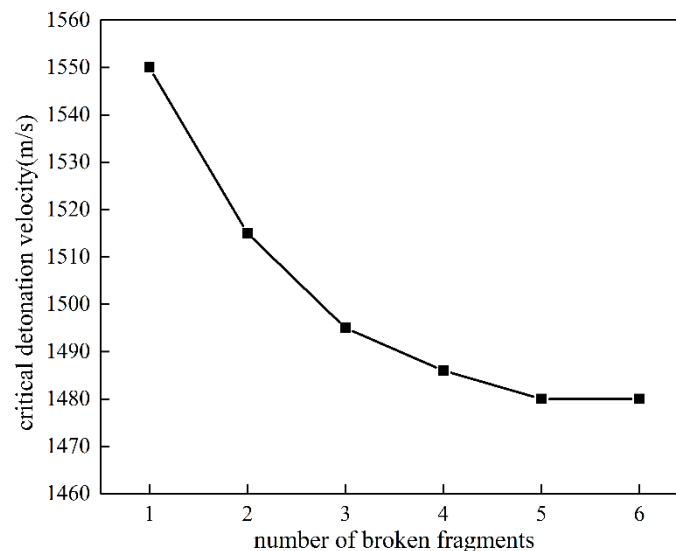


**Figure 12.** Multiple fragment impact critical detonation velocity curve.

As shown in Figure 12, as the number of standard fragments increases, the critical detonation speed decreases. However, when the number of fragments in the simulation model is more than five, the impact on the critical detonation velocity is no longer obvious. By analyzing the multiple fragment impact process, it can be seen that the shock wave is generated at the impact of the fragment. Shock waves generated by multiple impacts meet as they propagate through the propellant, raising the shock wave pressure, which

is equivalent to raising the overall shock wave input pressure. This makes the composite propellant more prone to shock-to-burst, which reduces the critical detonation velocity of the fragmentation impact. However, when the number of standard fragments reaches a certain number, the shock wave interaction generated by the standard fragments farther apart is no longer obvious, so the impact on the critical detonation velocity is reduced.

### 3.2.3. Shell Material

Using the typical solid rocket engine metal shell materials 30CrMnSiA steel, D406A steel and 2024 aluminum as shell materials, the influence law of different shell materials on the composite propellant impact detonation was studied. The simulation model is consistent with Section 3.1, and a three-dimensional fluid–solid coupling model of the standard broken fragment impacting shell-mounted composite propellant is established. The model contains 677,146 mesh nodes and 638,080 hexahedral cells. The total calculation time is set to  $t = 30 \mu\text{s}$ , and the time step is  $\Delta t = 0.1 \mu\text{s}$ . The wave impedance of the metallic material is

$$Z = \rho_0 c \quad (7)$$

where  $Z$  is the wave impedance of the metal shell material and  $\rho_0$  and  $c$  are the density and volume speed of sound, respectively. The shock wave impedance of each metal material is calculated and obtained as in Table 9.

**Table 9.** Metal material shock wave impedance.

Metal Materials	$\rho_0/(\text{g}\cdot\text{cm}^{-3})$	Speed of Sound $c/(\text{m}\cdot\text{s}^{-1})$	Shock Wave Impedance $Z/(\text{kg}\cdot\text{m}^{-2}\cdot\text{s}^{-1})$
30CrMnSiA steel	7.85	5664	$4.4 \times 10^7$
D406A steel	7.60	5918	$4.5 \times 10^7$
7A04 aluminum	2.785	5330	$1.5 \times 10^7$

The geometry of the shell is consistently set in the simulation model, and only the shell material is a variable. The critical detonation velocity of the standard fragment impact varies with the shell material as shown in Table 10.

**Table 10.** Fragmentation impact critical detonation velocity.

Materials	Density $\rho_0/(\text{g}\cdot\text{cm}^{-3})$	Critical Detonation Velocity $V_{\text{cr}}/(\text{m}\cdot\text{s}^{-1})$
30CrMnSiA steel	7.85	1550
D406A steel	7.60	1960
7A04 aluminum alloy	2.785	1125

As can be seen from Table 10, compared with aluminum alloy and steel shells, as the shell material strength increases, the standard fragments penetrating the shell will decay more energy. The weaker the composite propellant is subjected to, the initial shock wave becomes weaker, and the more difficult the occurrence of shock to blast. That is, under the same loading strength and shell wall thickness conditions, and the greater the strength of the metal shell material, the more difficult it is for the composite propellant to be shock detonated.

### 3.2.4. Shell Thickness

A high-energy HTPB propellant impact detonation model with different shell wall thickness protection states was established. A numerical simulation model of standard fragment impact shell-mounted composite propellant was established by using TrueGrid software, as described in Section 3.1. The general metal solid rocket motor shell wall thickness is  $\delta = 1\sim 3 \text{ mm}$ , so the shell wall thickness is set as shown in Table 11.

**Table 11.** Shell wall thickness setting.

Shell Wall Thickness/ $\delta_i$	$\delta_1/\text{mm}$	$\delta_2/\text{mm}$	$\delta_3/\text{mm}$	$\delta_4/\text{mm}$	$\delta_5/\text{mm}$
Shell wall thickness value	1.0	1.5	2.0	2.5	3.0

The shell inner diameter  $\Phi 157$  mm and shell length  $L = 400$  mm of the high-energy HTPB propellant are kept constant in each case. The critical impact velocity  $V_{cr}$  of the fragmentation of the high-energy HTPB propellant when the detonation occurs is calculated. The impact detonation critical impact velocity with the shell wall thickness variation law is shown in Figure 13.

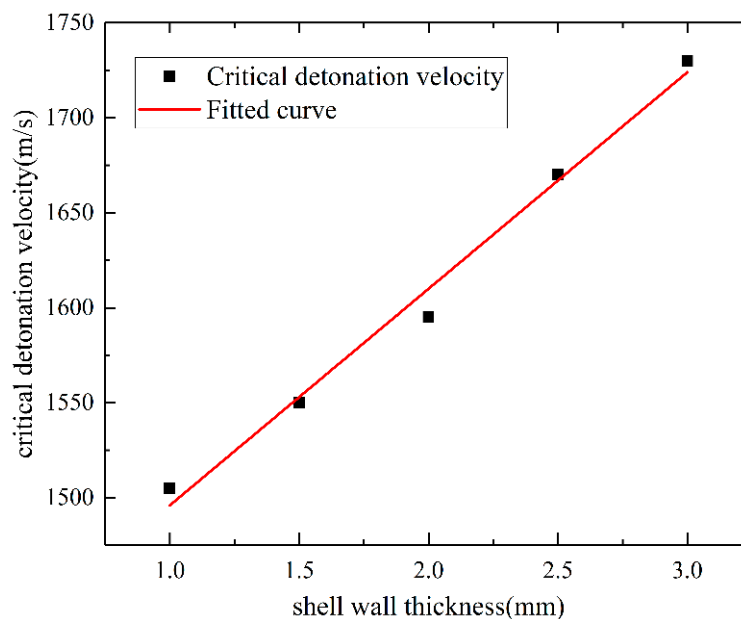
**Figure 13.** Impact detonation critical velocity with the shell wall thickness variation law.

Figure 13 shows that, as the shell wall thickness increases, the shock wave amplitude generated by the standard fragment on the shell surface becomes weaker. Therefore, the initial shock loading on the composite propellant becomes weaker, and it is more difficult for shock initiation to occur. The fitted equation was calculated to obtain

$$V_{cr} = 1382(1 + 0.082\delta) \quad (8)$$

where  $V_{cr}$  is a composite propellant impact detonation of the critical impact velocity of the standard fragments, unit:  $\text{m}\cdot\text{s}^{-1}$ ;  $\delta$  is the shell wall thickness, unit: mm; fitting formula applicable range:  $1.0 \text{ mm} \leq \delta \leq 3.0 \text{ mm}$ ; and fitting formula fit is  $R_2 = 0.98904$ .

#### 4. Conclusions

In this paper, the equation of state and the parameters of the reaction rate equation of the detonation product of high-energy HTPB four-component propellant were obtained by the cylinder test and the Lagrange test, combined with the genetic algorithm. Based on these parameters, the response process of high-energy HTPB engine under the effect of fragment impact was simulated and analyzed. The following conclusions were obtained:

- (1) Multiple fragment loading can increase the shock wave input pressure and reduce the critical detonation velocity of the fragment impacting high-energy four-component HTPB propellant. When the number of longitudinally distributed fragments is more than five, the critical detonation velocity no longer decreases with the increase in the number of fragments.

- (2) When the loading strength and shell wall thickness remains constant and the strength of the metal shell is greater, the more difficult it is for the composite propellant impact detonation to occur. In the case of wall thickness  $\delta = 1.5$  mm, the critical detonation velocity of 30CrMnSiA steel shell is  $V_{cr} = 1550$  m/s; the critical detonation velocity of the D406A steel shell is  $V_{cr} = 1960$  m/s; and the critical detonation velocity of the 7A04 aluminum alloy shell is  $V_{cr} = 1125$  m/s.
- (3) Under the conditions of loading strength and metal materials remaining constant, the greater the shell wall thickness, the more difficult for the composite propellant impact detonation. The relationship formula between fragment critical impact velocity and shell wall thickness is  $V_{cr} = 1382(1 + 0.082\delta)$  m/s.

**Author Contributions:** Conceptualization, J.N. and W.F.; methodology, Z.L. and J.N.; validation, W.F. and J.T.; formal analysis, Z.L. and J.N.; investigation, Z.L., F.J., T.G. and K.G.; resources, J.N.; data curation, Z.L., W.F. and J.T.; writing—original draft preparation, Z.L. and W.F.; writing—review and editing, J.N.; supervision, J.T. and T.G.; project administration, J.N.; funding acquisition, J.N. All authors have read and agreed to the published version of the manuscript.

**Funding:** This research received no external funding.

**Data Availability Statement:** The data that support the findings of this study are available from the corresponding author upon reasonable request.

**Conflicts of Interest:** The authors declare no conflict of interest.

## References

1. Song, L.F.; Li, H.X.; Zheng, Z.; Li, S.W.; Wu, Z. Research progress on the effect of fragments on the safety of solid propellant charges. *Aerodyn. Missile J.* **2019**, *1*, 92.
2. Salzman, P.K.; Irwin, O.R.; Andersen, W.H. Theoretical detonation characteristics of solid composite propellants. *AIAA J.* **1965**, *3*, 2230.
3. Bai, C.H.; Ding, J. Study of the shock initiation and the detonation process of composite propellants. *Explos. Shock. Waves* **1989**, *9*, 199.
4. Baker, P.J.; Coffey, C.S.; Mellor, A.M. Critical impact initiation energies for three HTPB propellants. *J. Propuls. Power* **1992**, *8*, 578. [[CrossRef](#)]
5. Huang, F.L.; Zhang, B.P. Study on the Detonation Danger of Solid Propellants. *J. Beijing Inst. Technol.* **2004**, *13*, 341.
6. Wu, J.Y.; Chen, L.; Lu, J.Y.; Feng, C.G.; Wang, Y.J. Research on shock initiation of the high energy solid propellants. *Acta Armamentarii* **2018**, *29*, 1315.
7. Bernecker, R.R. The deflagration-to-detonation transition process for high-energy propellants—a review. *AIAA J.* **1986**, *24*, 82. [[CrossRef](#)]
8. Liu, D.H.; Peng, P.G.; Wang, Z.F.; Pan, M.C. An investigation of the deflagration-to-detonation transition of the AP/HMX/HTPB composite propellant. *Acta Armamentarii* **1994**, *15*, 32.
9. Qin, N.; Liao, L.Q.; Jin, P.G.; Xu, H.Y.; Li, J.Q.; Fan, H.J. Experimental study on deflagration-to-detonation transition of several typical solid propellants. *Chin. J. Explos. Propellants* **2010**, *33*, 86.
10. Bowden, F.P.; Gurton, O.A. Birth and growth of the explosion in solids initiated by impact. *Nature* **1948**, *161*, 348. [[CrossRef](#)]
11. Price, D.; Clairmont, A.R. Explosive behavior of simplified propellant models. *Combust. Flame* **1977**, *29*, 87. [[CrossRef](#)]
12. Dick, J.J. Detonation initiation behavior of some HMX/AP/A1 propellants. *Combust. Flame* **1980**, *37*, 95. [[CrossRef](#)]
13. Kohga, M.; Shigi, D.; Beppu, M. Detonation properties of ammonium nitrate/nitramine-based composite propellants. *J. Energetic Mater.* **2019**, *37*, 309. [[CrossRef](#)]
14. Bai, C.H.; Ding, J. Reaction of solid propellants under shock loading. *Acta Armamentarii* **1991**, *12*, 38.
15. Yang, K.; Xu, B.H.; Guo, Y.Q.; Wu, Q. Calculation of detonation threshold of fragments impact on solid rocket motors. *J. Solid Rocket. Technol.* **2018**, *41*, 566.
16. Li, H.T.; Wu, Z.; Wang, Y.; Wang, Z.; Li, S.W.; Huang, Y.; Cheng, H.; Xu, S.; Song, L.F. Research Progresses of Experiment, Mechanism, and Formulas of Low Vulnerable Propellants under Mechanical Stimulations. *Equip. Environ. Eng.* **2019**, *16*, 57.
17. Lee, E.L. *Adiabatic Expansion of High Explosive Detonation Products*; UCRL250422; Univ. of California Radiation Lab. at Livermore: Livermore, CA, USA, 1965.
18. Lee, E.L.; Tarver, C.M. Phenomenological model of shock initiation in heterogeneous explosives. *Phys. Fluids* **1980**, *23*, 12. [[CrossRef](#)]
19. Zhang, W.; Xiao, X.K.; Wei, G. Constitutive relation and fracture model of 7A04 aluminum alloy. *Explos. Shock. Waves* **2011**, *31*, 81.
20. Li, Y.; Dong, M.H.S.; He, J.H.; Ye, K.C. Study on milling of 30CrMnSiA alloy steel based on abaqus. *Tool Eng.* **2016**, *50*, 35.

**Disclaimer/Publisher's Note:** The statements, opinions and data contained in all publications are solely those of the individual author(s) and contributor(s) and not of MDPI and/or the editor(s). MDPI and/or the editor(s) disclaim responsibility for any injury to people or property resulting from any ideas, methods, instructions or products referred to in the content.